Phase-field-based lattice Boltzmann finite-difference model for simulating thermocapillary flows

Haihu Liu[*] and Albert J. Valocchi

Department of Civil & Environmental Engineering, University of Illinois at Urbana-Champaign, Urbana, Illinois 61801, USA

Yonghao Zhang

Department of Mechanical & Aerospace Engineering, University of Strathclyde, Glasgow G1 1XJ, UK

Qinjun Kang

Earth and Environmental Sciences Division, Los Alamos National Laboratory, Los Alamos, New Mexico 87545, USA

A phase-field-based hybrid model that combines the lattice Boltzmann method with the finite difference method is proposed for simulating immiscible thermocapillary flows with variable fluid-property ratios. Using a phase field methodology, an interfacial force formula is analytically derived to model the interfacial tension force and the Marangoni stress. We present an improved lattice Boltzmann equation (LBE) method to capture the interface between different phases and solve the pressure and velocity fields, which can recover the correct Cahn-Hilliard equation (CHE) and Navier-Stokes equations. The LBE method allows not only use of variable mobility in the CHE, but also simulation of multiphase flows with high density ratio because a stable discretization scheme is used for calculating the derivative terms in forcing terms. An additional convection-diffusion equation is solved by the finite difference method for spatial discretization and the Runge-Kutta method for time marching to obtain the temperature field, which is coupled to the interfacial tension through an equation of state. The model is first validated against analytical solutions for the thermocapillary driven convection in two superimposed fluids at negligibly small Reynolds and Marangoni numbers. It is then used to simulate thermocapillary migration of a three-dimensional deformable droplet and bubble at various Marangoni numbers and density ratios, and satisfactory agreement is obtained between numerical results and theoretical predictions.

I. INTRODUCTION

Thermocapillary convection is a phenomenon of fluid movement that arises as a consequence of the variation of interfacial tension at a fluid-fluid interface caused by temperature differences. It can be employed as a mechanism for driving the motion of droplets and bubbles immersed in a second fluid. For most fluids the interfacial tension is a decreasing function of the temperature, and the induced thermcapillary stresses (also called Marangoni stresses [1]) lead to the movement of droplets or bubbles from the regions of low temperature, where the interfacial tension is high, to the warmer regions, where the interfacial tension is low. The thermocapillary motion of droplets and bubbles plays an important role in many natural physical processes as well as numerous industrial activities, particularly in space material processing and many other engineering and scientific applications under microgravity conditions where sedimentation and gravity-driven convection are largely eliminated. Thus, it attracts an increasing amount of research interest worldwide along with the progress of human space technology. For example, Hadland *et al.* [2] and Kang *et al.* [3] conducted experimental studies on the thermocapillary migration of air bubbles in silicone oil aboard a NASA space shuttle and the 22nd Chinese recoverable satellite *RS-22,* respectively, and both experiments covered a wide range of flow and thermal conditions. In recent years, optically actuated thermocapillary forces have been used for manipulating the dynamic behavior of droplets or bubbles in

microfluidic devices [4–10], where bulk phenomena can be negligible in comparison with interfacial effects due to large surface-to-volume ratio and low Reynolds number. Such optically controlled actuation is advantageous over convectional hydrodynamic stress [11–14], electrohydrodynamic force [15–17], and resistive heating [18–20] methods for droplet and bubble manipulations, as it is easier to address a large array of droplets/bubbles using optical patterns [7]. Furthermore, optically controlled actuation is contactless and dynamically reconfigurable, without any additional requirement on microchip fabrication [21]. For a comprehensive review of these topics, interested readers are referred to the excellent book by Subramanian and Balasubramanian [22] as well as the book chapter by Robert de Saint Vincent and Delville [23].

Numerical modeling and simulations can be very instrumental in enhancing understanding of thermocapillary flows because one can obtain detailed information about flow field such as temperature and velocity distribution. However, numerical simulation of thermocapillary flows is a challenging task, where the capillary effect usually plays a dominant role. Discretization errors in calculation of interfacial forces may generate unphysical spurious velocities which can cripple the velocity field in the whole computational domain. Minimizing the spurious velocities at the interface still remains a major challenge for numerical models and algorithms. Due to the strong dependence of interfacial tension on temperature, the temperature fluctuations result in nonuniform interfacial tension forces and Marangoni stresses that affect the flow field at the interface, which in turn alter the interfacial temperature distribution through the induced interfacial flows. While the front-tracking method is not suitable for simulating

---

[*]haihuliu@illinois.edu

interface breaking and coalescing because the interface must be manually ruptured based upon some *ad hoc* criteria [24], interface capturing methods such as volume-of-fluid and level set methods will suffer from numerical instability at the interface region when the interfacial tension becomes a dominant factor in microdroplet or -bubble behavior [25]. Microscopically, the phase segregation and the interfacial dynamics between different phases are due to interparticle forces or interactions [26,27]. Thus, mesoscopic level models are expected to describe accurately the complex dynamic behavior of multiphase flows.

The lattice Boltzmann method (LBM) is known to be capable of modeling interfacial interactions while incorporating fluid flow as a system feature [28]. It is a pseudo-molecular method that tracks evolution of the distribution function of an assembly of molecules and is built upon microscopic models and mesoscopic kinetic equations [29]. Its mesoscopic nature can provide many of the advantages of molecular dynamics, making the LBM especially effective for simulation of complex interfacial flows. However, the currently available LBMs mainly focus on simulating multiphase flows with a constant interfacial tension [26,30–34], so they are unable to simulate thermocapillary flows around moving and stationary interfaces except our recently improved color-fluid model [35], in which a concept of continuum surface force (CSF) is used to model the interfacial tension force and Marangoni stress, and the phase segregation is achieved through the recoloring algorithm proposed by Latva-Kokko and Rothman [36]. However, this model can only simulate thermocapillary flows with equal density. In addition, it is restricted to using the same specific heat for both fluids because a simplified temperature equation is solved in the framework of LBM. These deficiencies largely limit its prospect for practical applications.

In this work a phase-field-based hybrid model combining the LBM and the finite difference method (FDM) is presented to simulate immiscible thermocapillary flows with variable fluid-property ratios. Based on the free energy theory, an interfacial force formula is derived analytically to model the interfacial tension force and the Marangoni stress. An improved lattice Boltzmann equation (LBE) method is employed to capture the interface between different phases and solve the pressure and velocity fields, which can recover the correct Cahn-Hilliard equation (CHE) and Navier-Stokes equations (NSEs). The LBE method allows not only use of variable mobility, but also simulation of immiscible binary fluids with high density ratio because a stable discretization scheme [33,34] is used for calculating derivative terms appeared in forcing terms. In addition, a convection-diffusion equation is solved by the FDM for spatial discretization and the Runge-Kutta (RK) method for time marching to obtain temperature, which is coupled to the interfacial tension by an equation of state. A series of numerical simulations are carried out to examine the capability and accuracy of the hybrid model.

II. THEORY AND MATHEMATICAL MODEL

Phase field methods are a particular class of diffuse-interface models that are becoming increasingly popular for modeling multiphase flows. A unifying feature of all the phase field methods is the existence of a free energy functional, which not only determines the equilibrium properties, but also strongly influences the dynamics of a multiphase system. The free energy is described by a conserved order parameter, e.g., the relative concentration of the two phases in a binary fluid, which varies continuously over a thin interfacial layer and is mostly uniform in the bulk phases. In phase field methods, sharp interfaces are replaced by thin but nonzero thickness transition regions where the interfacial forces are smoothly distributed [37], so that the numerical computation of interface movement and deformation can be carried out on fixed grids.

A. Phase field theory and governing equations for hydrodynamics

We consider here an incompressible system of two nominally immiscible Newtonian fluids. The order parameter ϕ is introduced to identify the regions where two fluid flows occur: $\phi = -1$ is occupied by fluid 1 and $\phi = 1$ by fluid 2. The interface is represented by $\phi = 0$ with an interfacial layer of thickness ϵ. Denoting the fluid domain by Ω, one can write the free energy of the system as [38]

$$\mathscr{F}(\phi, \boldsymbol{\nabla}\phi) = \int_{\Omega}\left(\Psi(\phi) + \frac{\epsilon^2}{2}|\boldsymbol{\nabla}\phi|^2\right)d\Omega, \qquad (1)$$

where $\Psi(\phi)$ is the bulk free energy density and takes a double-well form $\Psi(\phi) = \frac{1}{4}(\phi^2 - 1)^2$. The term $\frac{\epsilon^2}{2}|\boldsymbol{\nabla}\phi|^2$ accounts for the excess free energy in the interfacial region.

The chemical potential μ is defined as the variational derivative of the free energy with respect to the order parameter, i.e.,

$$\mu = \frac{\delta\mathscr{F}}{\delta\phi} = \frac{d\Psi(\phi)}{d\phi} - \epsilon^2\nabla^2\phi = \phi^3 - \phi - \epsilon^2\nabla^2\phi. \quad (2)$$

The equilibrium interface profile can be obtained from Eq. (2) at $\mu = 0$. The one-dimensional solution of this equation is

$$\phi(z) = \tanh\left(\frac{z}{\sqrt{2}\epsilon}\right), \qquad (3)$$

where z is the spatial location normal to the interface ($z = 0$).

The scalar field of the order parameter is advected by the fluid velocity $\mathbf{u}$, while being diffused due to the gradient of chemical potential. The time evolution of the order parameter is governed by the convective CHE

$$\frac{\partial\phi}{\partial t} + \mathbf{u}\cdot\boldsymbol{\nabla}\phi = \boldsymbol{\nabla}\cdot(M\boldsymbol{\nabla}\mu), \qquad (4)$$

where $M > 0$ is the mobility or Onsager coefficient. In the classical CHE [39], the mobility is a constant, whereas in this study it depends on the order parameter through $M = M_c\sqrt{(1 - \phi^2)^2}$, where M_c is a constant. Compared with a constant mobility, the variable mobility can significantly reduce the numerical dissipation around small droplets or bubbles to yield physically acceptable results [40]. At the solid walls, we impose the following no-flux boundary conditions [41]:

$$\mathbf{n}_w\cdot\boldsymbol{\nabla}\phi = 0 \quad \text{and} \quad \mathbf{n}_w\cdot M\boldsymbol{\nabla}\mu = 0, \qquad (5)$$

where $\mathbf{n}_w$ is the unit vector normal to the solid wall.

It is well known that the expression for the stress jump across the interface Σ is given by Ref. [35]

$$[\mathbf{T}\cdot\mathbf{n}]_{\Sigma} = \mathbf{T}\cdot\mathbf{n}|_{\Sigma,2} - \mathbf{T}\cdot\mathbf{n}|_{\Sigma,1} = \sigma\kappa\mathbf{n} - \boldsymbol{\nabla}_S\sigma, \qquad (6)$$

where $\mathbf{T} = -p\mathbf{I} + \eta(\nabla\mathbf{u} + \nabla\mathbf{u}^T)$ is the stress tensor, p is the pressure, η is the dynamic viscosity, $\mathbf{I}$ is the second-order identity tensor, σ is the local interfacial tension parameter, $\mathbf{n}$ is the unit vector normal to Σ and directed towards fluid 2, $\kappa = \nabla \cdot \mathbf{n}$ is the local interface curvature, and $\nabla_S = (\mathbf{I} - \mathbf{n} \otimes \mathbf{n}) \cdot \nabla$ is the surface gradient operator. The first term on the right-hand side of Eq. (6) is the interfacial tension force and the second term is the Marangoni stress. In order to induce the local stress jump across the interface, a volume-distributed interfacial force $\mathbf{F}_S$, should be added in the momentum equation as an additional body force. The interfacial force is

$$\mathbf{F}_S = (-\sigma\kappa\mathbf{n} + \nabla_S\sigma)\delta_\Sigma, \tag{7}$$

where δ_Σ is the Dirac δ function used to localize the force explicitly at the interface, which should satisfy

$$\int_{-\infty}^{\infty} \delta_\Sigma \, dz = 1 \tag{8}$$

in order to recover properly the stress jump condition, Eq. (6), in the sharp-interface limit.

Based on the order parameter, the interface normal can be expressed as $\vec{n} = \frac{\nabla\phi}{|\nabla\phi|}$. In addition, we choose the Dirac δ function as $\delta_\Sigma = \frac{3\sqrt{2}}{4}\epsilon|\nabla\phi|^2$, which leads to

$$\mathbf{F}_S = \frac{3\sqrt{2}}{4}\epsilon|\nabla\phi|^2(-\sigma\kappa\mathbf{n} + \nabla_S\sigma). \tag{9}$$

After some vector calculus and algebraic manipulations, Eq. (9) can be further simplified as (see Appendix for the derivation)

$$\mathbf{F}_S = \frac{3\sqrt{2}}{4}\epsilon\nabla \cdot [\sigma(T)(|\nabla\phi|^2\mathbf{I} - \nabla\phi \otimes \nabla\phi)]. \tag{10}$$

Note that the expression of interfacial force, i.e., Eq. (10), is derived based on the free energy of double-well form, in which the interface profile is given exactly by Eq. (3). Other forms of free energy (or equation of state) can give such a profile approximately only in the vicinity of the critical point.

In a thermocapillary flow, an equation of state is required to relate the interfacial tension to the temperature, which may be linear or nonlinear. For the sake of simplicity, we consider only a linear relation between the interfacial tension and the temperature in this study [35,42], i.e.,

$$\sigma(T) = \sigma_{\text{ref}} + \sigma_T(T - T_{\text{ref}}), \tag{11}$$

where T_{ref} is the reference temperature, σ_{ref} is the interfacial tension at T_{ref}, and σ_T is the rate of change of interfacial tension with temperature, defined as $\sigma_T = \partial\sigma/\partial T$.

With the interfacial force $\mathbf{F}_S$ given by Eq. (10), the governing equations for the incompressible fluid flows can

be written as [41,43]

$$\nabla \cdot \mathbf{u} = 0, \tag{12}$$

$$\rho\left(\frac{\partial\mathbf{u}}{\partial t} + \mathbf{u} \cdot \nabla\mathbf{u}\right) = -\nabla p + \nabla \cdot [\eta(\nabla\mathbf{u} + \nabla\mathbf{u}^T)] + \mathbf{F}_S, \tag{13}$$

where ρ is the fluid density, which is taken as a function of the order parameter:

$$\rho = \frac{1-\phi}{2}\rho_1 + \frac{1+\phi}{2}\rho_2, \tag{14}$$

where ρ_1 and ρ_2 are the densities of fluid 1 and fluid 2 at saturation, respectively.

B. Lattice Boltzmann method for solution of hydrodynamic equations

The NSEs, Eqs. (12) and (13), and the CHE, Eq. (4), are solved using the LBE model proposed by Lee and Liu [34]. In this model, two distribution functions are employed: one is the order parameter distribution function, which is used to capture the interface between different phases, and the other is the pressure distribution function for solving the pressure and fluid momentum. Following a similar argument as pointed out recently by Li *et al.* [44], this model cannot recover the correct momentum equation, i.e., Eq. (13), using the Chapman-Enskog multiscale expansion. In addition, we will demonstrate that the target CHE, i.e., Eq. (4) cannot be recovered exactly in the model of Lee and Liu [34], which also stems from the error term appeared in the momentum equation. In this section, we will present an improved LBE model, in which some additional terms are introduced to obtain the correct NSEs and CHE.

In this model, the pressure and fluid momentum are solved through a pressure distribution function, which is defined by $g_\alpha = f_\alpha c_s^2 + (p - \rho c_s^2)\Gamma_\alpha(0)$, where c_s is the speed of sound which is given by $c_s = c/\sqrt{3}$ with $c = \delta_x/\delta_t$ being the lattice speed and δ_x being the lattice length, f_α is the density distribution function in the α direction, and $\Gamma_\alpha(\mathbf{u}) = \Gamma_\alpha = w_\alpha(1 + \frac{\mathbf{e}_\alpha \cdot \mathbf{u}}{c_s^2} + \frac{(\mathbf{e}_\alpha \cdot \mathbf{u})^2}{2c_s^4} - \frac{|\mathbf{u}|^2}{2c_s^2})$. For D2Q9 and D3Q19 models used in this study, the lattice velocity $\mathbf{e}_\alpha$ and the weight coefficient w_α are given as follows:

D2Q9:

$$\mathbf{e}_i = \begin{cases} (0,0), & i = 0; \\ (\pm1,0)c, (0,\pm1)c, & i = 1,2,3,4; \\ (\pm1,\pm1)c, & i = 5,6,7,8. \end{cases} \tag{15}$$

$$w_i = \begin{cases} 4/9, & i = 0; \\ 1/9, & i = 1,2,3,4; \\ 1/36, & i = 5,6,7,8; \end{cases} \tag{16}$$

D3Q19:

$$\mathbf{e}_i = \begin{cases} (0,0,0), & i = 0; \\ (\pm1,0,0)c, (0,\pm1,0)c, (0,0,\pm1)c, & i = 1,2,\ldots,6; \\ (\pm1,\pm,0)c, (\pm1,0,\pm1)c, (0,\pm1,\pm1)c, & i = 7,8,\ldots,18. \end{cases} \tag{17}$$

$$w_i = \begin{cases} 1/3, & i = 0; \\ 1/18, & i = 1,2,\ldots,6; \\ 1/36, & i = 7,8,\ldots,18. \end{cases} \tag{18}$$

The time evolution equation for f_α, using the standard BGK (Bhatnagar-Gross-Krook) approximation, is written as [26,33,34]

$$\frac{Df_\alpha}{Dt} = \frac{\partial f_\alpha}{\partial t} + \mathbf{e}_\alpha \cdot \nabla f_\alpha$$
$$= -\frac{1}{\lambda}\left(f_\alpha - f_\alpha^{\mathrm{eq}}\right) + \frac{(\mathbf{e}_\alpha - \mathbf{u}) \cdot \mathbf{F}}{c_s^2}\Gamma_\alpha, \quad (19)$$

where λ is the relaxation time, $f_\alpha^{\mathrm{eq}} = \rho\Gamma_\alpha$ is the equilibrium distribution function, and $\mathbf{F}$ is the intermolecular force, which is defined as

$$\mathbf{F} = \nabla\rho c_s^2 - \nabla p + \mathbf{F}_S + \mathbf{F}_a, \quad (20)$$

in which $\mathbf{F}_a = \frac{\rho_2 - \rho_1}{2}\nabla \cdot (M\nabla\mu)\mathbf{u}$ is an additional force term [44], which is absent in the original model of Lee and Liu [34]. Based on the original model of Lee and Liu, it can be shown using the Chapman-Enskog multiscale expansion that the following momentum equation can be recovered in the low Mach number limit

$$\frac{\partial(\rho\mathbf{u})}{\partial t} + \nabla \cdot (\rho\mathbf{u} \otimes \mathbf{u}) = -\nabla p + \nabla \cdot [\eta(\nabla\mathbf{u} + \nabla\mathbf{u}^T)] + \mathbf{F}_S, \quad (21)$$

which is different from the target momentum equation, i.e., Eq. (13), and the error term is $\mathbf{u}(\frac{\partial\rho}{\partial t} + \mathbf{u} \cdot \nabla\rho)$. From Eqs. (4) and (14), we can rewrite the error term as $\mathbf{u}(\frac{\partial\rho}{\partial t} + \mathbf{u} \cdot \nabla\rho) = \frac{\rho_2 - \rho_1}{2}\nabla \cdot (M\nabla\mu)\mathbf{u}$. Clearly, the error term is nonzero when there is density difference between two fluids. Thus, the additional force term $\mathbf{F}_a$ is introduced in Eq. (20) in order to eliminate the error term. According to Eqs. (19) and (20), the evolution equation for g_α can be written as

$$\frac{\partial g_\alpha}{\partial t} + \mathbf{e}_\alpha \cdot \nabla g_\alpha = -\frac{1}{\lambda}\left(g_\alpha - g_\alpha^{\mathrm{eq}}\right) + (\mathbf{e}_\alpha - \mathbf{u})$$
$$\cdot \left\{\nabla\rho c_s^2[\Gamma_\alpha - \Gamma_\alpha(0)] + \mathbf{F}_S + \mathbf{F}_a\right\}, \quad (22)$$

where $g_\alpha^{\mathrm{eq}} = f_\alpha^{\mathrm{eq}}c_s^2 + (p - \rho c_s^2)\Gamma_\alpha(0)$. Note that the pressure gradient ∇p is dropped in Eq. (22) considering it is the order of $O(\mathrm{Ma}^2)$ for incompressible flows [33,34], where $\mathrm{Ma} = U/c_s$ is the Mach number with U being the characteristic velocity of the system.

The fluid interfaces are captured by the order parameter distribution function h_α, which is related to f_α by $h_\alpha = \frac{\phi}{\rho}f_\alpha$ and $h_\alpha^{\mathrm{eq}} = \frac{\phi}{\rho}f_\alpha^{\mathrm{eq}}$. Following the work of Lee and his coworker [34,45], the evolution equation for h_α is given by

$$\frac{\partial h_\alpha}{\partial t} + \mathbf{e}_\alpha \cdot \nabla h_\alpha = -\frac{1}{\lambda}\left(h_\alpha - h_\alpha^{\mathrm{eq}}\right) + \nabla \cdot (M\nabla\mu)\Gamma_\alpha$$
$$+ (\mathbf{e}_\alpha - \mathbf{u}) \cdot \left[\nabla\phi - \frac{\phi}{\rho c_s^2}(\nabla p - \mathbf{F}_S)\right]. \quad (23)$$

The macrodynamic behavior arising from the LBE, Eq. (23), can be found from a multi-scale analysis using a small expansion parameter ε, which is proportional to the Knudsen number (ratio of the molecular mean free path to the characteristic length scale). To do this, we introduce the following expansions:

$$h_\alpha = h_\alpha^{\mathrm{eq}} + \varepsilon h_\alpha^{(1)} + \varepsilon^2 h_\alpha^{(2)} + \cdots, \quad (24)$$

$$\partial_t = \varepsilon\partial_{t_0} + \varepsilon^2\partial_{t_1}, \quad \nabla = \varepsilon\nabla_1, \quad (25)$$

$$\mathbf{F}_S = \varepsilon\mathbf{F}_{S1}. \quad (26)$$

Substituting Eqs. (24)–(26) into Eq. (23), the equations for the first- and second-order expansions in ε become

$$O(\varepsilon^1): \quad \left(\partial_{t_0} + \mathbf{e}_\alpha \cdot \nabla_1\right)h_\alpha^{\mathrm{eq}}$$
$$= -\frac{h_\alpha^{(1)}}{\lambda} + \nabla_1 \cdot (M\nabla\mu)\Gamma_\alpha + (\mathbf{e}_\alpha - \mathbf{u})$$
$$\cdot \left[\nabla_1\phi - \frac{\phi}{\rho c_s^2}(\nabla_1 p - \mathbf{F}_{S1})\right]\Gamma_\alpha \quad (27)$$

and

$$O(\varepsilon^2): \quad \partial_{t_1}h_\alpha^{\mathrm{eq}} + \left(\partial_{t_0} + \mathbf{e}_\alpha \cdot \nabla_1\right)h_\alpha^{(1)} = -\frac{h_\alpha^{(2)}}{\lambda}. \quad (28)$$

The zeroth-order moment of Eq. (27) leads to

$$\partial_{t_0}\phi + \nabla_1 \cdot (\mathbf{u}\phi) = \nabla_1 \cdot (M\nabla\mu). \quad (29)$$

Substituting $h_\alpha^{(1)}$ from Eq. (27) into Eq. (28) and taking zeroth-order moment of Eq. (28), we obtain that

$$\partial_{t_1}\phi - \lambda\nabla_1 \cdot \left\{\frac{\phi}{\rho}\left[\rho\left(\partial_{t_0}\mathbf{u} + \mathbf{u} \cdot \nabla_1\mathbf{u}\right) + \nabla_1 p - \mathbf{F}_{S1}\right]\right\} = 0, \quad (30)$$

which can be written as

$$\partial_{t_1}\phi = 0, \quad (31)$$

when Eq. (22) is applied. Hence, the target CHE can be recovered correctly by adding ε times Eq. (29) and ε^2 times Eq. (31). However, the correct CHE cannot be recovered in the original model of Lee and Liu [34], where Eq. (30) cannot lead to Eq. (31) because one can only obtain the following equality:

$$\partial_{t_0}(\rho\mathbf{u}) + \nabla_1 \cdot (\rho\mathbf{u} \otimes \mathbf{u}) + \nabla_1 p - \mathbf{F}_{S1} = 0. \quad (32)$$

The LBEs for Eqs. (22) and (23) can be obtained by employing the Crank-Nicolson integration in time along

characteristics [34]:

$$g_\alpha(\mathbf{x} + \mathbf{e}_\alpha \delta_t, t + \delta_t) = g_\alpha(\mathbf{x},t) - \frac{g_\alpha - g_\alpha^{\mathrm{eq}}}{2\tau}\bigg|_{(\mathbf{x},t)} - \frac{g_\alpha - g_\alpha^{\mathrm{eq}}}{2\tau}\bigg|_{(\mathbf{x} + \mathbf{e}_\alpha \delta_t, t + \delta_t)} + \frac{\delta_t}{2}(\mathbf{e}_\alpha - \mathbf{u}) \cdot \left\{ \nabla^{\mathrm{BD}} \rho c_s^2 [\Gamma_\alpha - \Gamma_\alpha(0)] + (\mathbf{F}_S + \mathbf{F}_a)\Gamma_\alpha \right\}\bigg|_{(\mathbf{x},t)}$$

$$+ \frac{\delta_t}{2}(\mathbf{e}_\alpha - \mathbf{u}) \cdot \left\{ \nabla^{\mathrm{CD}} \rho c_s^2 [\Gamma_\alpha - \Gamma_\alpha(0)] + (\mathbf{F}_S + \mathbf{F}_a)\Gamma_\alpha \right\}\bigg|_{(\mathbf{x} + \mathbf{e}_\alpha \delta_t, t + \delta_t)}, \tag{33}$$

$$h_\alpha(\mathbf{x} + \mathbf{e}_\alpha \delta_t, t + \delta_t) = h_\alpha(\mathbf{x},t) - \frac{h_\alpha - h_\alpha^{\mathrm{eq}}}{2\tau}\bigg|_{(\mathbf{x},t)} - \frac{h_\alpha - h_\alpha^{\mathrm{eq}}}{2\tau}\bigg|_{(\mathbf{x} + \mathbf{e}_\alpha \delta_t, t + \delta_t)} + \frac{\delta_t}{2}\nabla \cdot (M\nabla\mu)\Gamma_\alpha\bigg|_{(\mathbf{x},t)} + \frac{\delta_t}{2}\nabla \cdot (M\nabla\mu)\Gamma_\alpha\bigg|_{(\mathbf{x} + \mathbf{e}_\alpha \delta_t, t + \delta_t)}$$

$$+ \frac{\delta_t}{2}(\mathbf{e}_\alpha - \mathbf{u}) \cdot \left[\nabla^{\mathrm{BD}}\phi - \frac{\phi}{\rho c_s^2}(\nabla^{\mathrm{BD}} p - \mathbf{F}_S) \right] \Gamma_\alpha\bigg|_{(\mathbf{x},t)}$$

$$+ \frac{\delta_t}{2}(\mathbf{e}_\alpha - \mathbf{u}) \cdot \left[\nabla^{\mathrm{CD}}\phi - \frac{\phi}{\rho c_s^2}(\nabla^{\mathrm{BD}} p - \mathbf{F}_S) \right] \Gamma_\alpha\bigg|_{(\mathbf{x} + \mathbf{e}_\alpha \delta_t, t + \delta_t)}, \tag{34}$$

where the dimensionless relaxation time $\tau = \lambda/\delta_t$ and is related to the kinematic viscosity by $\nu = \tau c_s^2 \delta_t$. The superscripts "BD" and "CD" denote the second-order biased difference and the second-order central difference, respectively, which are introduced to enhance numerical stability in simulating high-density ratio flows. As suggested by Lee and Liu [34], the directional derivatives (of a variable φ) are evaluated by

$$\delta_t \mathbf{e}_\alpha \cdot \nabla^{\mathrm{CD}} \varphi|_{(\mathbf{x})} = \tfrac{1}{2}[\varphi(\mathbf{x} + \mathbf{e}_\alpha \delta_t) - \varphi(\mathbf{x} - \mathbf{e}_\alpha \delta_t)], \tag{35}$$

$$\delta_t \mathbf{e}_\alpha \cdot \nabla^{\mathrm{BD}} \varphi|_{(\mathbf{x})} = \tfrac{1}{2}[4\varphi(\mathbf{x} + \mathbf{e}_\alpha \delta_t) - \varphi(\mathbf{x} + 2\mathbf{e}_\alpha \delta_t) - 3\varphi(\mathbf{x})], \tag{36}$$

and derivatives other than the directional derivatives can be obtained by taking moments of the directional derivatives with appropriate weights. The first- and second-order derivatives are calculated as

$$\nabla^{\mathrm{CD}} \varphi|_{(\mathbf{x})} = \frac{1}{2c_s^2 \delta_t} \sum_\alpha w_\alpha \mathbf{e}_\alpha [\varphi(\mathbf{x} + \mathbf{e}_\alpha \delta_t) - \varphi(\mathbf{x} - \mathbf{e}_\alpha \delta_t)], \tag{37}$$

$$\nabla^{\mathrm{BD}} \varphi|_{(\mathbf{x})} = \frac{1}{2c_s^2 \delta_t} \sum_\alpha w_\alpha \mathbf{e}_\alpha [4\varphi(\mathbf{x} + \mathbf{e}_\alpha \delta_t) - \varphi(\mathbf{x} + 2\mathbf{e}_\alpha \delta_t) - 3\varphi(\mathbf{x})], \tag{38}$$

$$\nabla^2 \varphi|_{(\mathbf{x})} = \frac{1}{c_s^2 \delta_t^2} \sum_\alpha w_\alpha [\varphi(\mathbf{x} + \mathbf{e}_\alpha \delta_t) - 2\varphi(\mathbf{x}) + \varphi(\mathbf{x} - \mathbf{e}_\alpha \delta_t)]. \tag{39}$$

By introducing a modified distribution functions $\bar{g}_\alpha$ and its equilibrium distribution $\bar{g}_\alpha^{\mathrm{eq}}$,

$$\bar{g}_\alpha = g_\alpha + \frac{1}{2\tau}\left(g_\alpha - g_\alpha^{\mathrm{eq}}\right) - \frac{\delta_t}{2}(\mathbf{e}_\alpha - \mathbf{u}) \cdot \left\{ \nabla^{\mathrm{CD}} \rho c_s^2 [\Gamma_\alpha - \Gamma_\alpha(0)] + (\mathbf{F}_S + \mathbf{F}_a)\Gamma_\alpha \right\}, \tag{40}$$

$$\bar{g}_\alpha^{\mathrm{eq}} = g_\alpha^{\mathrm{eq}} - \frac{\delta_t}{2}(\mathbf{e}_\alpha - \mathbf{u}) \cdot \left\{ \nabla^{\mathrm{CD}} \rho c_s^2 [\Gamma_\alpha - \Gamma_\alpha(0)] + (\mathbf{F}_S + \mathbf{F}_a)\Gamma_\alpha \right\}, \tag{41}$$

Eq. (33) can be written in a simpler form as

$$\bar{g}_\alpha(\mathbf{x} + \mathbf{e}_\alpha \delta_t, t + \delta_t) = \bar{g}_\alpha(\mathbf{x},t) - \frac{1}{\tau + 1/2}\left(\bar{g}_\alpha - \bar{g}_\alpha^{\mathrm{eq}}\right)\bigg|_{(\mathbf{x},t)}$$
$$+ \delta_t(\mathbf{e}_\alpha - \mathbf{u}) \cdot \left\{ \nabla^{\mathrm{MD}} \rho c_s^2 [\Gamma_\alpha - \Gamma_\alpha(0)] + (\mathbf{F}_S + \mathbf{F}_a)\Gamma_\alpha \right\}\big|_{(\mathbf{x},t)}, \tag{42}$$

where the superscript "MD" denotes the second-order mixed difference defined as

$$\delta_t \mathbf{e}_\alpha \cdot \nabla^{\mathrm{MD}} \varphi = \tfrac{1}{2}(\delta_t \mathbf{e}_\alpha \cdot \nabla^{\mathrm{CD}} \varphi + \delta_t \mathbf{e}_\alpha \cdot \nabla^{\mathrm{BD}} \varphi), \tag{43}$$

$$\nabla^{\mathrm{MD}} \varphi = \tfrac{1}{2}(\nabla^{\mathrm{CD}} \varphi + \nabla^{\mathrm{BD}} \varphi). \tag{44}$$

Similarly, Eq. (34) is recast as

$$\bar{h}_\alpha(\mathbf{x} + \mathbf{e}_\alpha \delta_t, t + \delta_t)$$
$$= \bar{h}_\alpha(\mathbf{x},t) + \frac{\delta_t}{2}\nabla \cdot (M\nabla\mu)\Gamma_\alpha\bigg|_{(\mathbf{x},t)}$$
$$+ \frac{\delta_t}{2}\nabla \cdot (M\nabla\mu)\Gamma_\alpha\bigg|_{(\mathbf{x} + \mathbf{e}_\alpha \delta_t, t)} + \delta_t(\mathbf{e}_\alpha - \mathbf{u})$$
$$\cdot \left[\nabla^{\mathrm{MD}}\phi - \frac{\phi}{\rho c_s^2}(\nabla^{\mathrm{MD}} p - \mathbf{F}_S) \right] \Gamma_\alpha\bigg|_{(\mathbf{x},t)}, \tag{45}$$

where

$$\bar{h}_\alpha = h_\alpha + \frac{1}{2\tau}\left(h_\alpha - h_\alpha^{\mathrm{eq}}\right) - \frac{\delta_t}{2}(\mathbf{e}_\alpha - \mathbf{u})$$
$$\cdot \left[\nabla^{\mathrm{CD}}\phi - \frac{\phi}{\rho c_s^2}(\nabla^{\mathrm{CD}} p - \mathbf{F}_S) \right] \Gamma_\alpha, \tag{46}$$

$$\bar{h}_\alpha^{\mathrm{eq}} = h_\alpha^{\mathrm{eq}} - \frac{\delta_t}{2}(\mathbf{e}_\alpha - \mathbf{u}) \cdot \left[\nabla^{\mathrm{CD}}\phi - \frac{\phi}{\rho c_s^2}(\nabla^{\mathrm{CD}} p - \mathbf{F}_S) \right] \Gamma_\alpha. \tag{47}$$

Note that the term $\frac{\delta_t}{2}\nabla \cdot (M\nabla\mu)|_{(\mathbf{x} + \mathbf{e}_\alpha \delta_t, t + \delta_t)}$ is replaced explicitly by its value at the previous time step t, as suggested in Ref. [34]. In addition, $\tau = 1/2$ is chosen in Eq. (45)

considering the fact that the recovered CHE is independent of the choice of τ as indicated by Eqs. (27) and (31).

The order parameter, the hydrodynamic pressure and the fluid velocity are calculated by taking the zeroth- and the first-order moments of the modified distribution functions:

$$\phi = \sum_{\alpha} \bar{h}_{\alpha}, \quad (48)$$

$$\mathbf{u} = \left(\frac{1}{c_s^2} \sum_{\alpha} \bar{g}_{\alpha} \mathbf{e}_{\alpha} + \frac{\delta_t}{2} \mathbf{F}_S \right) \bigg/ \left[\rho - \frac{\delta_t}{4}(\rho_2 - \rho_1)\nabla \cdot (M\nabla\mu) \right], \quad (49)$$

$$p = \sum_{\alpha} \bar{g}_{\alpha} + \frac{\delta_t}{2} \mathbf{u} \cdot \nabla^{\mathrm{CD}}\rho c_s^2. \quad (50)$$

C. Finite difference method for solution of temperature equation

The solution of the flow problem requires information about the temperature field, T. When the viscous dissipation and compression work done by the pressure are negligible, the temperature evolution can be governed by

$$\rho c_p \left(\frac{\partial T}{\partial t} + \mathbf{u} \cdot \nabla T \right) = \nabla \cdot (k\nabla T), \quad (51)$$

where c_p and k are the specific heat and the thermal conductivity of fluid mixture, respectively, and calculated as a function of the order parameter, i.e.,

$$c_p = \frac{1 - \phi}{2} c_{p_1} + \frac{1 + \phi}{2} c_{p_2}, \quad (52)$$

$$k = \frac{1 - \phi}{2} k_1 + \frac{1 + \phi}{2} k_2, \quad (53)$$

where the subscripts 1 and 2 denote the values of the physical properties in fluid 1 and fluid 2, respectively. Note Eq. (51) can be solved in the LBM framework if there are no jumps in ρ and c_p across the fluid interface [35]. However, to our best knowledge, no LBM is currently available to recover the correct temperature equation, i.e., Eq. (51), when the densities and the specific heats in both fluids are unequal.

Equation (51) can be rewritten as

$$\frac{\partial T}{\partial t} = -\mathbf{u} \cdot \nabla T + \frac{1}{\rho c_p}(\nabla k \cdot \nabla T + k\nabla^2 T) \equiv \mathbb{L}(T), \quad (54)$$

where the finite difference method is used to discretize the spatial derivatives. In order to ensure high accuracy and consistency, Eqs. (37) and (39) are applied for calculating the gradient and Laplacian terms, respectively. We employ the explicit RK method for time stepping of Eq. (54). During the time marching from t^n to t^{n+1} ($=t^n + \delta_t$), the fluid velocity ($\mathbf{u}$), density (ρ), specific heat (c_p), and thermal conductivity (k) are kept fixed. Similar treatments have been commonly used in various LBM-FDM hybrid models [46–49]. In particular, when the fourth-order RK method is chosen, the time stepping follows the following steps:

$$\hbar_1 = \delta_t \mathbb{L}(t^n, T^n), \quad \hbar_2 = \delta_t \mathbb{L}\left(t^n + \tfrac{1}{2}\delta_t, T^n + \tfrac{1}{2}\hbar_1\right),$$

$$\hbar_3 = \delta_t \mathbb{L}\left(t^n + \tfrac{1}{2}\delta_t, T^n + \tfrac{1}{2}\hbar_2\right),$$

$$\hbar_4 = \delta_t \mathbb{L}(t^n + \delta_t, T^n + \hbar_3),$$

$$T^{n+1} = T^n + \tfrac{1}{6}(\hbar_1 + 2\hbar_2 + 2\hbar_3 + \hbar_4). \quad (55)$$

Note that the choice of the fourth-order RK method is not imperative. We have found that use of the second-order RK method produces equally accurate results.

III. NUMERICAL RESULTS

Thermocapillary motion of droplets or bubbles can be characterized by several important dimensionless parameters, including Reynolds number (Re), Marangoni number (Ma), capillary number (Ca), fluid density ratio ($\tilde{\rho}$), viscosity ratio ($\tilde{\eta}$), thermal conductivity ratio ($\tilde{k}$), and specific heat ratio ($\tilde{c}_p$). Without losing generality, we choose the fluid 2 as the continuous phase in this study, so the dimensionless parameters are defined as follows:

$$\mathrm{Re} = \frac{LU}{\nu_2}, \quad \mathrm{Ma} = \frac{\rho_2 c_{p_2} LU}{k_2} = \mathrm{Re} \cdot \mathrm{Pr}, \quad \mathrm{Ca} = \frac{U\eta_2}{\sigma_{\mathrm{ref}}}, \quad (56)$$

$$\tilde{\rho} = \frac{\rho_1}{\rho_2}, \quad \tilde{\eta} = \frac{\eta_1}{\eta_2}, \quad \tilde{k} = \frac{k_1}{k_2}, \quad \tilde{c}_p = \frac{c_{p_1}}{c_{p_2}}, \quad (57)$$

where L and U are the characteristic length and velocity of the system, respectively, and Pr is the Prandtl number.

A. Thermocapillary flows in a heated microchannel with two superimposed planar fluids

The model is first used to investigate the thermocapillary driven flow in a heated microchannel with two superimposed planar fluids [50]. The setup of the problem is shown in Fig. 1. The heights of the upper fluid 1 and the lower fluid 2 are a and b, respectively, while the fluids extend to infinity in the horizontal direction. We impose a uniform temperature to the upper wall and a sinusoidal temperature (which is higher than that of the upper wall) to the lower wall as

$$T(x,a) = T_c \quad (58)$$

and

$$T(x,-b) = T_h + T_0 \cos(\omega x), \quad (59)$$

respectively, where $0 < T_0 < T_c < T_h$, and $\omega = \frac{2\pi}{l}$ is a wave number with l being a length scale. The above temperature boundary conditions establish a periodic temperature field in the horizontal direction with a period length of l. Therefore, one needs only to consider the solution in one period domain with $-\frac{l}{2} \leqslant x < \frac{l}{2}$.
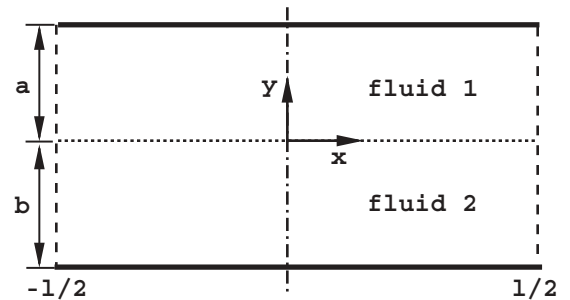
FIG. 1. The geometric setup depicting two immiscible fluids in a microchannel. The temperatures of the lower and upper walls are $T(x,-b) = T_h + T_0 \cos(\omega x)$ and $T(x,a) = T_c$, respectively, where $T_h > T_c > T_0$ and $\omega = \frac{2\pi}{l}$ is a wave number.

With the characteristic length and velocity defined as $L = b$ and $U = \frac{|\sigma_T|T_0}{l}\frac{b}{\eta_2}$ respectively, one can easily calculate Re, Ma, and Ca through Eq. (56). Assuming Re $\ll 1$, Ma $\ll 1$, and Ca $\ll 1$, the interface is thought to remain flat, and the momentum and energy equations can be simplified to be linear. By solving the simplified governing equations with the stress boundary condition [Eq. (6)] at the interface, analytical solutions for temperature and velocity fields were obtained recently by Pendse and Esmaeeli [50] as

$$T^A(x,y) = \frac{(T_c - T_h)y + \tilde{k}T_c b + T_h a}{a + \tilde{k}b}$$
$$+ T_0 f(\tilde{a},\tilde{b},\tilde{k}) \sinh(\tilde{a} - \omega y)\cos(\omega x), \quad (60)$$

$$u_x^A(x,y) = U_{\max}\left\{\left[C_1^a + \omega(C_2^a + C_3^a y)\right]\cosh(\omega y)\right.$$
$$\left. + (C_3^a + \omega C_1^a y)\sinh(\omega y)\right\}\sin(\omega x), \quad (61)$$

$$u_y^A(x,y) = -\tilde{k}U_{\max}\left[C_1^a y\cosh(\omega y) + (C_2^a + C_3^a y)\sinh(\omega y)\right]$$
$$\times \cos(\omega x), \quad (62)$$

in the upper fluid 1 and

$$T^A(x,y) = \frac{\tilde{k}(T_c - T_h)y + \tilde{k}T_c b + T_h a}{a + \tilde{k}b}$$
$$+ T_0 f(\tilde{a},\tilde{b},\tilde{k})[\sinh(\tilde{a})\cosh(\omega\tilde{y})$$
$$- \tilde{k}\sinh(\omega y)\cosh(\tilde{a})]\cos(\omega x), \quad (63)$$

$$u_x^A(x,y) = U_{\max}\left\{\left[C_1^b + \omega(C_2^b + C_3^b y)\right]\cosh(\omega y)\right.$$
$$\left. + (C_3^b + \omega C_1^b y)\sinh(\omega y)\right\}\sin(\omega x), \quad (64)$$

$$u_y^A(x,y) = -\tilde{k}U_{\max}\left[C_1^b y\cosh(\omega y) + (C_2^b + C_3^b y)\sinh(\omega y)\right]$$
$$\times \cos(\omega x), \quad (65)$$

in the lower fluid 2. In the above equations, the unknown constants are determined by

$$\tilde{a} = a\omega; \quad \tilde{b} = b\omega, \quad (66)$$

$$f(\tilde{a},\tilde{b},\tilde{k}) = [\tilde{k}\sinh(\tilde{b})\cosh(\tilde{a}) + \sinh(\tilde{a})\cosh(\tilde{b})]^{-1}, \quad (67)$$

$$C_1^a = \frac{\sinh^2(\tilde{a})}{\sinh^2(\tilde{a}) - \tilde{a}^2}; \quad C_2^a = \frac{-a\tilde{a}}{\sinh^2(\tilde{a}) - \tilde{a}^2};$$
$$C_3^a = \frac{2\tilde{a} - \sinh(2\tilde{a})}{2[\sinh^2(\tilde{a}) - \tilde{a}^2]}, \quad C_1^b = \frac{\sinh^2(\tilde{b})}{\sinh^2(\tilde{b}) - \tilde{b}^2}; \quad (68)$$
$$C_2^b = \frac{-b\tilde{b}}{\sinh^2(\tilde{b}) - \tilde{b}^2}; \quad C_3^b = \frac{\sinh(2\tilde{b}) - 2\tilde{b}}{2[\sinh^2(\tilde{b}) - \tilde{b}^2]},$$

and

$$U_{\max} = -\left(\frac{T_0\sigma_T}{\eta_2}\right)g(\tilde{a},\tilde{b},\tilde{k})h(\tilde{a},\tilde{b},\tilde{\eta}), \quad (69)$$

where

$$g(\tilde{a},\tilde{b},\tilde{k}) = \sinh f(\tilde{a},\tilde{b},\tilde{k}) \quad (70)$$

and

$$h(\tilde{a},\tilde{b},\tilde{\eta}) = \frac{[\sinh^2(\tilde{a}) - \tilde{a}^2][\sinh^2(\tilde{b}) - \tilde{b}^2]}{\tilde{\eta}[\sinh^2(\tilde{b}) - \tilde{b}^2][\sinh(2\tilde{a}) - 2\tilde{a}] + [\sinh^2(\tilde{a}) - \tilde{a}^2][\sinh(2\tilde{b}) - 2\tilde{b}]}. \quad (71)$$

We carry out the numerical simulations in a two-dimensional computational domain with the channel length $l = 160$ lattice unit (lu), and the initial heights of fluid layer $a = b = 40$ lu. Periodic boundary conditions are applied on the left and right boundaries of the domain. On the upper and lower walls, no-slip boundary conditions are imposed, and the wall temperatures are specified through Eqs. (58) and (59), where $T_h = 20$, $T_c = 10$ and $T_0 = 4$. In addition, the no-flux boundary conditions, given by Eq. (5), are also enforced on the solid walls. Specifically, we introduce two additional grid layers (AGLs) outside the fluid domain. The values of the order parameter in AGLs are taken as the mirror image of ϕ in the fluid nodes. For example, for the lower wall ($y = -b$), the order parameter in the AGLs are given by

$$\phi(x,-b-\delta_x) = \phi(x,-b+\delta_x),$$
$$\phi(x,-b-2\delta_x) = \phi(x,-b+2\delta_x), \quad (72)$$

which leads to

$$\mu(x,-b-\delta_x) = \mu(x,-b+\delta_x). \quad (73)$$

Thus, the no-flux boundary conditions can be satisfied exactly. The fluid properties and numerical parameters are chosen as $\sigma_T = -5 \times 10^{-4}$, $T_{\rm ref} = 10$, $\sigma_{\rm ref} = 2.5 \times 10^{-2}$, $\eta_{1,2} = 0.2$,

$k_2 = 0.2$, $\epsilon = \sqrt{2}$ and $M_c = 5 \times 10^{-2}$. These values result in Re, Ma and Ca of typical value of $O(0.01)$ or at most $O(0.1)$. To indicate the effect of the thermal conductivity ratio on induced flow and temperature, both $\tilde{k} = 1$ and $\tilde{k} = 1/5$ are simulated. In each case, the system reaches its steady state after a number of iterations. The relative L^2-norm errors for the temperature and velocity fields are measured at the steady state between our computed results and the analytical solutions as given by Eqs. (60)–(65); the relative errors are defined as

$$E_T = \frac{\sum_{\mathbf{x}}\|T(\mathbf{x}) - T^A(\mathbf{x})\|}{\sum_{\mathbf{x}}\|T^A(\mathbf{x})\|} \quad (74)$$

for temperature and

$$E_v = \frac{\sum_{\mathbf{x}}\|\mathbf{u}(\mathbf{x}) - \mathbf{u}^A(\mathbf{x})\|}{\sum_{\mathbf{x}}\|\mathbf{u}^A(\mathbf{x})\|} \quad (75)$$

for velocity, respectively.

Figure 2 shows equispaced contours of temperature field for two different thermal conductivity ratios: (a) $\tilde{k} = 1$ and (b) $\tilde{k} = 1/5$. We can clearly observe that our computed results (the solid-line contours) are in good agreement with the analytical solutions (the dashed-line contours) with the relative errors $E_T = 2.25 \times 10^{-4}$ and 5.23×10^{-3} for $\tilde{k} = 1$ and $1/5$,

(a) $\tilde{k} = 1$
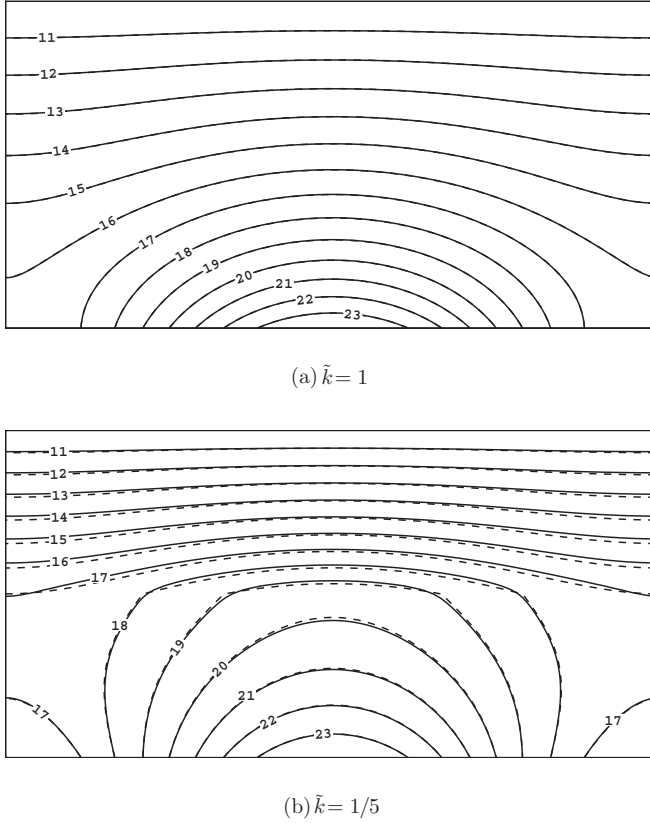
(b) $\tilde{k} = 1/5$

FIG. 2. Temperature contours for fluid systems with thermal conductivity ratios of (a) $\tilde{k} = 1$ and (b) $\tilde{k} = 1/5$. Simulation results and the analytical solution are represented by the solid and dashed lines, respectively, labeled with temperature values.

(a) $\tilde{k} = 1$

(b) $\tilde{k} = 1/5$

FIG. 3. (Color online) Velocity vectors for fluid systems with thermal conductivity ratios of (a) $\tilde{k} = 1$ and (b) $\tilde{k} = 1/5$. Velocity vectors are shown at every third grid point. Simulation results and the analytical solutions are represented by the red and light green lines with an arrow, respectively.

respectively. It should be noted that our computed isotherms slightly deviate from the analytical ones for $\tilde{k} = 1/5$, which is due to the finite interface thickness of our phase field model and the jump of thermal conductivity across the interface. At a low thermal conductivity ratio, i.e., $\tilde{k} = 1/5$, the isotherms become denser in the upper fluid. Also, the isotherms approaching from the lower fluid tend to be normal to the interface, implying that heat transfer between the lower fluid and the interface in the y direction is close to zero. Figure 3 shows the comparison of velocity vectors between our computed results and the analytical solutions for $\tilde{k} = 1$ and $1/5$, and the corresponding relative errors are $E_v = 5.71 \times 10^{-2}$ and 8.41×10^{-2}. The computed velocity vectors agree well with the analytical counterparts except those close to the interface at $\tilde{k} = 1/5$, consistent with the deviation in temperature contours. Finally, it can be found by comparing Figs. 3(a) with 3(b) that the thermocapillary-driven convection will be strengthened with decreasing thermal conductivity ratio.

B. Thermocapillary migration of deformable droplets and bubbles

In microgravity environment, the thermocapillary migration of droplets or bubbles in the ambient liquid is caused by the nonuniform interfacial tension induced by the imposed temperature gradient. Thermocapillary migration was first analyzed by Young *et al.* [51] in the case of infinitesimal

Reynolds and Marangoni numbers, in which convective transport of momentum and energy can be neglected compared to molecular transport of these quantities. They derived a theoretical expression for the migration velocity (also known as YGB velocity) of a spherical droplet or bubble (fluid 1) in a constant temperature gradient, ∇T_∞, within an unbounded fluid medium (fluid 2):

$$U_{\text{YGB}} = \frac{2U}{(2 + 3\tilde{\eta})(2 + \tilde{k})}. \tag{76}$$

Here U is the characteristic velocity defined by the balance of the thermocapillary force and the viscous force on the droplet or bubble as follows:

$$U = -\frac{\sigma_T |\nabla T_\infty| R}{\eta_2}, \tag{77}$$

where R is the radius of the droplet or bubble, which is chosen as the characteristic length to define Reynolds and Marangoni numbers.

A droplet of radius $R = 20$ lu is placed inside of a three-dimensional box of size $8R \times 8R \times 16R$. The center of droplet is initially located at the center of the three-dimensional computational box. No-slip boundary conditions are imposed on the top and bottom walls, and periodic boundary conditions are used in the x and y directions (the side faces). A linear temperature field is imposed in the z direction, with $T = 0$ on the bottom wall and $T = 32$ on the top wall, resulting in $|\nabla T_\infty| = 0.1$. In order to test the accuracy of the proposed
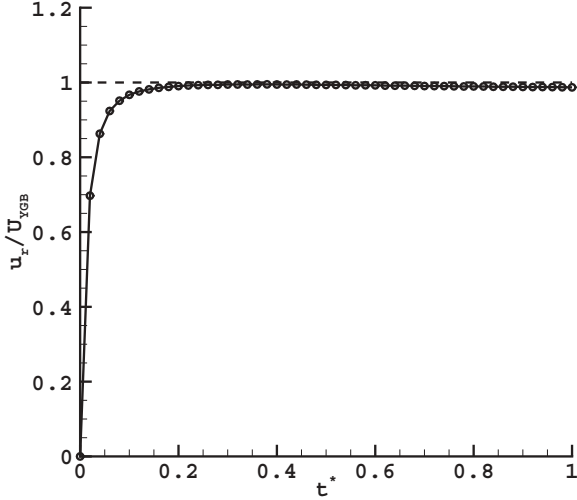
FIG. 4. Time evolution of normalized migration velocity of a 3D spherical droplet at Ma = Re = 0.1. The dashed line represents the analytical prediction of YGB theory in the limit of vanishing Reynolds and Marangoni numbers, while the solid line with open circles is our simulation result.

hybrid model, the numerical simulation is first carried out with the fluid properties of $\rho_{1,2} = c_{p_{1,2}} = 1$, $\eta_{1,2} = k_{1,2} = 0.2$, $T_{\text{ref}} = 16$, $\sigma_{\text{ref}} = 2.5 \times 10^{-3}$, and $\sigma_T = -10^{-4}$. Using these values, the theoretical value of the migration velocity is $U_{\text{YGB}} = 1.33\bar{3} \times 10^{-4}$, and the Reynolds and Marangoni numbers are 0.1. In the simulations, the migration velocity u_r of droplet or bubble is calculated by

$$u_r(t) = \frac{\int_V \phi u_z \, dV}{\int_V \phi \, dV} = \frac{\sum_{\mathbf{x}} u_z(\mathbf{x},t)\phi(\mathbf{x},t)}{\sum_{\mathbf{x}} \phi(\mathbf{x},t)}, \quad \text{where } \phi < 0. \tag{78}$$

Figure 4 shows the temporal evolution of the computed migration velocity normalized by U_{YGB} for the test case of Ma = Re = 0.1. The dimensionless time is defined as $t^* = Ut/R$. Obviously, our simulation result is in excellent quantitative agreement with the analytical prediction of Young *et al.* [51] represented by the dashed line since the effects of convective transport of momentum and energy are negligible in this test case. Note that the relative error E is defined as $E = \frac{|u_r - U_{\text{YGB}}|}{U_{\text{YGB}}} \times 100\%$, and here its value is around 0.8%.

Having established the accuracy of the proposed numerical model, we carry out numerical simulations to study thermocapillary migration of a deformable droplet at large Marangoni numbers, for which analytical results are not available. Figure 5 presents the evolutions of the normalized migration velocity for three different Marangoni numbers, i.e., Ma = 1, 10, and 100, at a constant Reynolds number of 1. The different Marangoni numbers are achieved by adjusting k_1 and k_2 while keeping $k_1 = k_2$. We also choose $\nu_{1,2} = 0.1$, $\sigma_T = -2.5 \times 10^{-4}$ and $\sigma_{\text{ref}} = 5 \times 10^{-3}$, and keep all the other physical properties the same as those in the above test case. The early transient of droplet motion exhibits the same characteristics as those reported by Oliver and De Witt [52] and Welch [53], which is caused by the initial conditions used in our numerical simulations, i.e., $\mathbf{u}|_{t=0} = 0$ and $T|_{t=0} = z|\nabla T_\infty|$. The thermocapillary migration can reach a steady state for
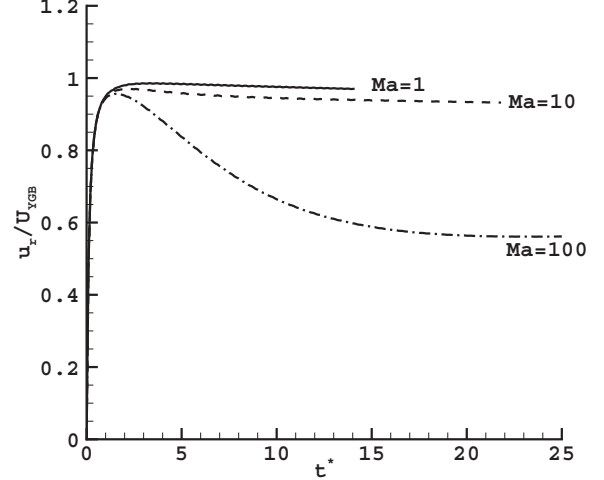
FIG. 5. Time evolutions of droplet migration velocity at different Marangoni numbers for Re = 1.

all Marangoni numbers under consideration. It is evidenced that the terminal migration velocity decreases monotonically with the Marangoni number, which is consistent with the previous theoretical and numerical studies for the case of non-deformable droplets or bubbles [52,54–56]. The dependence of the terminal migration velocity on the Marangoni number can be explained by the isotherms surrounding the droplet in x-z meridian plane, which are shown in Fig. 6, where the temperature value is labeled on each contour. Obviously, the enhanced convective transport of energy with the increase of the Marangoni number results in the wrapping of the isotherms around the front of the droplet (also, the thermal boundary layer in front of the droplet becomes increasingly thin), leading to a substantial reduction of the temperature gradient at the droplet interface. Small average temperature gradient at the interface will reduce the driving force for the droplet migration. Figure 6 also depicts the corresponding velocity vectors in a coordinate system moving with the droplet centroid. Relative to the migrating droplet, the flow pattern within the droplet exhibits recirculation flow that is similar to the Hills spherical vortex [57]. It can be clearly seen that the vortex intensity weakens as the Marangoni number increases.

In order to show the capability of the present model for multiphase flows with high liquid-to-gas density ratio, we simulate thermocapillary migration of gas bubble (fluid 1) in a liquid medium (fluid 2) for four different density ratios, i.e., $\tilde{\rho} = 1:10$, 1:50, 1:100 and 1:200. The initial radius of bubble is fixed at $R = 20$ lu, and the geometric setup and boundary conditions are kept the same as those in the cases of droplet migration. The different density ratios are achieved by varying the gas density while the liquid density is fixed at 1. In these simulations, the constant fluid properties are taken as $\nu_{1,2} = 0.2$, $\sigma_{\text{ref}} = 2.5 \times 10^{-4}$, $\sigma_T = -10^{-5}$, $k_2 = 0.2$, $c_{p_1} = 2$ and $c_{p_2} = 5$, leading to Re = 0.01 and Ma = 0.05. Note that we also choose the Prandtl numbers of gas and liquid as $\text{Pr}_1 = 1$ and $\text{Pr}_2 = 5$, and thus the thermal conductivity of gas phase should be changed accordingly for different density ratios. In simulations we have observed that the numerical values of the order parameter may not exactly lie within the range $[-1,1]$. The order parameter value may be slightly out
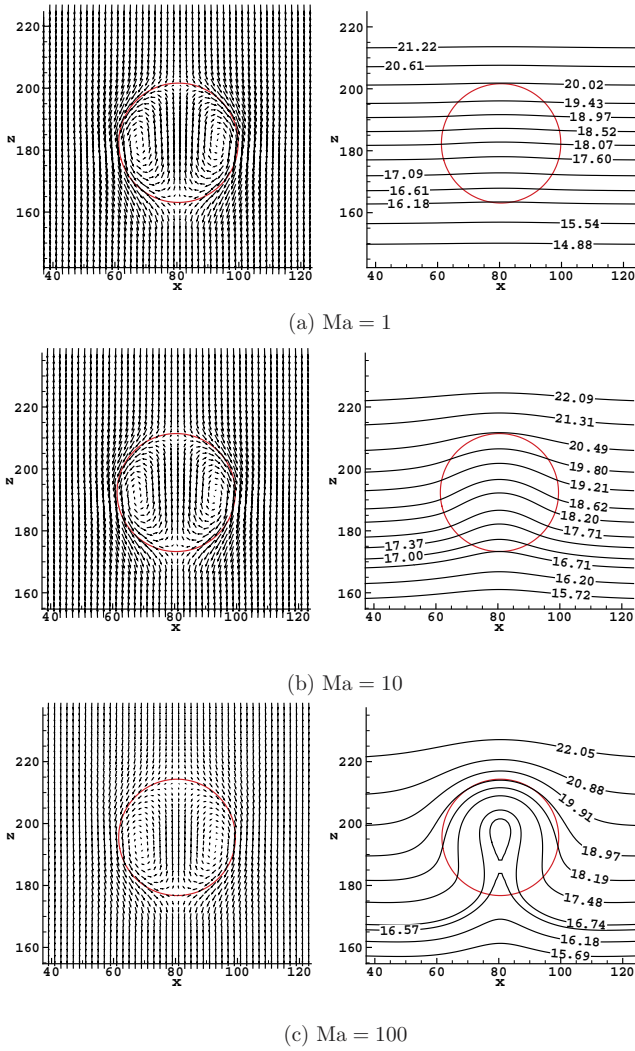
(a) Ma = 1

(b) Ma = 10

(c) Ma = 100

FIG. 6. (Color online) Velocity vectors (the left figures) and temperature fields (the right figures) around the rising droplet in the x-z meridian plane at (a) Ma = 1, (b) Ma = 10, and (c) Ma = 100. Note that the velocity vectors are plotted in a reference frame moving with the droplet.

of bound at some lattice sites (e.g., by $\sim 10^{-3}$), which may induce numerical instability if the density ratio of liquid to gas is high. Similar to Ref. [34], for high liquid-to-gas density ratios we introduce an artificial free energy that acts as an "energy" obstacle to avoid $\phi < -1$:

$$\Psi_A(\phi) = \begin{cases} \beta_A(\phi+1)^2, & \text{if } \phi < -1, \\ 0, & \text{otherwise.} \end{cases} \quad (79)$$

Thus, the chemical potential needs to be replaced by $\mu + \partial\Psi_A/\partial\phi$ to carry the effect of the artificial energy obstacle. In our simulations, the coefficient in Ψ_A is taken as $\beta_A = 20.0$.

Figure 7 presents the evolution of bubble migration velocity normalized by U for the four cases. All cases except the lowest $\tilde\rho$ exhibit a similar evolution characteristic as the one with equal density shown above, whereas for $\tilde\rho = 1{:}200$ (the uppermost line in Fig. 7) a slight overshoot in bubble migration velocity is observed in the early stage. We can also see that the terminal bubble velocity increases with decreasing $\tilde\rho$. For
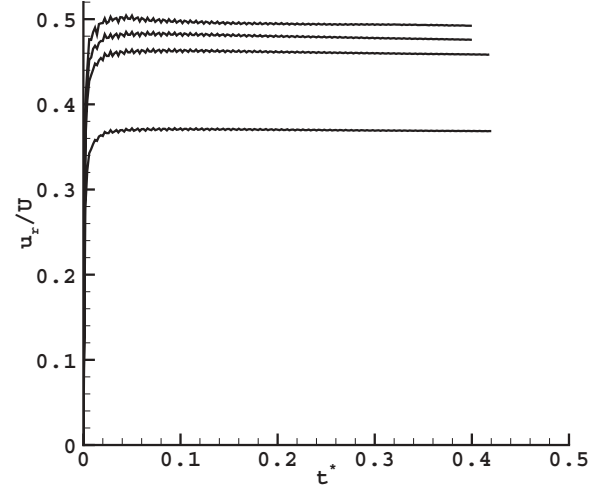
FIG. 7. Time evolutions of bubble migration velocity at different density ratios for $\tilde\eta = \tilde\rho$, $\tilde{c}_p = 0.4$, $\frac{\text{Pr}_1}{\text{Pr}_2} = 0.2$, Re = 0.01, and Ma = 0.05. The values of density ratio are $\tilde\rho = 1/10$, $1/50$, $1/100$, and $1/200$ for the lines from bottom to top.

$\tilde\rho = \{\frac{1}{10}, \frac{1}{50}, \frac{1}{100}, \frac{1}{200}\}$, the calculated results of the terminal bubble velocity (u_r) are 3.72×10^{-5}, 4.62×10^{-5}, 4.8×10^{-5} and 4.94×10^{-5}, respectively, which can be comparable to the theoretical YGB velocities (see Table I). This indicates that our hybrid LBM-FDM model can provide satisfactory numerical prediction of the thermocapillary flows with various density ratios. In Fig. 7 we also notice some velocity oscillations in the initial stages. As shown by Amaya-Bower and Lee [58], who numerically studied a single bubble rising due to buoyancy, grid resolution can affect the amplitude of velocity oscillation during the rise of a bubble. This is also reflected in Fig. 8, which gives the comparison of bubble migration velocity between two different grid resolutions for $\tilde\rho = 1{:}100$, where the lower line is the result of coarse grid with $R = 20$ lattices while the upper one is the result of fine grid with $R = 30$ lattices. It can be clearly seen that, grid refinement can decrease the velocity oscillation to some extent although velocity oscillations are observed for both grid resolutions. It is therefore believed that the oscillations observed in Fig. 7 are numerical artifacts rather than physical phenomena. Note that the velocity oscillations are also observed even for two-phase fluids with equal density when the color-fluid model is applied for thermocapillary migration [35]. In addition, Fig. 8 indicates that the grid refinement can only slightly improve the simulation results, so we compromise and use $R = 20$ lattices to avoid high computational cost. Figure 9 shows the steady-state isotherms around the moving bubble and the corresponding velocity

TABLE I. Comparison of terminal bubble velocity between YGB theory and our LBM-FDM simulations for various density ratios.

$\tilde\rho$	U_{YGB}	u_r	Relative error (E)
1:10	3.95×10^{-5}	3.72×10^{-5}	5.82%
1:50	4.76×10^{-5}	4.62×10^{-5}	2.94%
1:100	4.88×10^{-5}	4.80×10^{-5}	1.64%
1:200	4.94×10^{-5}	4.94×10^{-5}	0
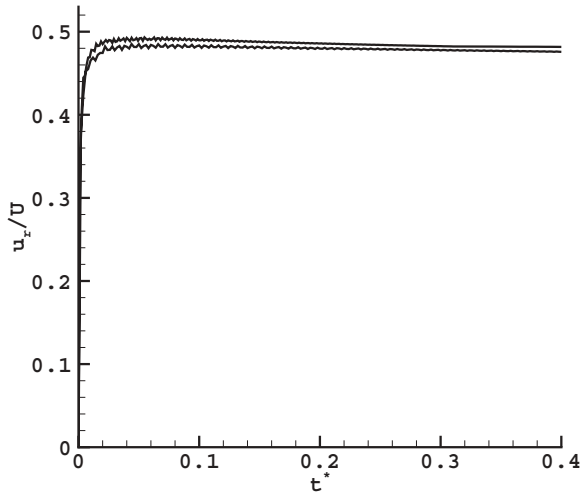
FIG. 8. Time evolutions of bubble migration velocity at different grid resolutions for $\tilde{\rho} = \tilde{\eta} = \frac{1}{100}$, $\tilde{c}_p = 0.4$, $\frac{\mathrm{Pr}_1}{\mathrm{Pr}_2} = 0.2$, Re = 0.01, and Ma = 0.05. The upper line represents the simulation result of fine grid with $R = 30$ lattices, and the lower line represents the simulation result of coarse grid with $R = 20$ lattices.

fields plotted in a coordinate system moving with the bubble centroid in the x-z meridian plane for (a) $\tilde{\rho} = 1{:}10$, (b) $\tilde{\rho} = 1{:}50$, (c) $\tilde{\rho} = 1{:}100$, and (d) $\tilde{\rho} = 1{:}200$. All four cases show similar velocity and temperature fields, even though the bubble migration velocities are different. The spacings between two isotherms in the bubble and the external liquid are markedly different, which is caused by the big difference in the thermal conductivity.

In this model, we have used a stable discretization scheme for estimating the gradient operators in forcing terms, which is able to enhance the numerical stability for solving high density ratio multiphase flows. However, several recent studies showed that this scheme does not conserve the total mass of a system and is non-Galilean invariant due to the discretization errors [59–62]. This is also true for our model but we observe less than 0.5% change in the total mass of the system from its initial value for each case.

IV. CONCLUSIONS

A hybrid LBM-FDM numerical model based on phase field theory is proposed to simulate immiscible thermocapillary flows with variable density ratio and other fluid properties. The interfacial forces, including the interfacial tension force and the Marangoni stress, are modeled using a phase field methodology. The diffuse interfaces are evolved through the CHE. The NSEs and the CHE are solved by an improved LBE method originally proposed by Lee and Liu [34], in which an additional force term is introduced in order to recover the correct momentum equation and CHE. This method uses a stable discretization technique for derivative terms, enabling it to handle high-density ratio multiphase flows. This method also allows us to use variable mobility, which can suppress effectively the dissolution of small droplets or bubbles. In addition, a convection-diffusion equation is solved through the FDM combining with four-order RK method for time

(a) $\tilde{\rho} = 1{:}10$

(b) $\tilde{\rho} = 1{:}50$

(c) $\tilde{\rho} = 1{:}100$

(d) $\tilde{\rho} = 1{:}200$
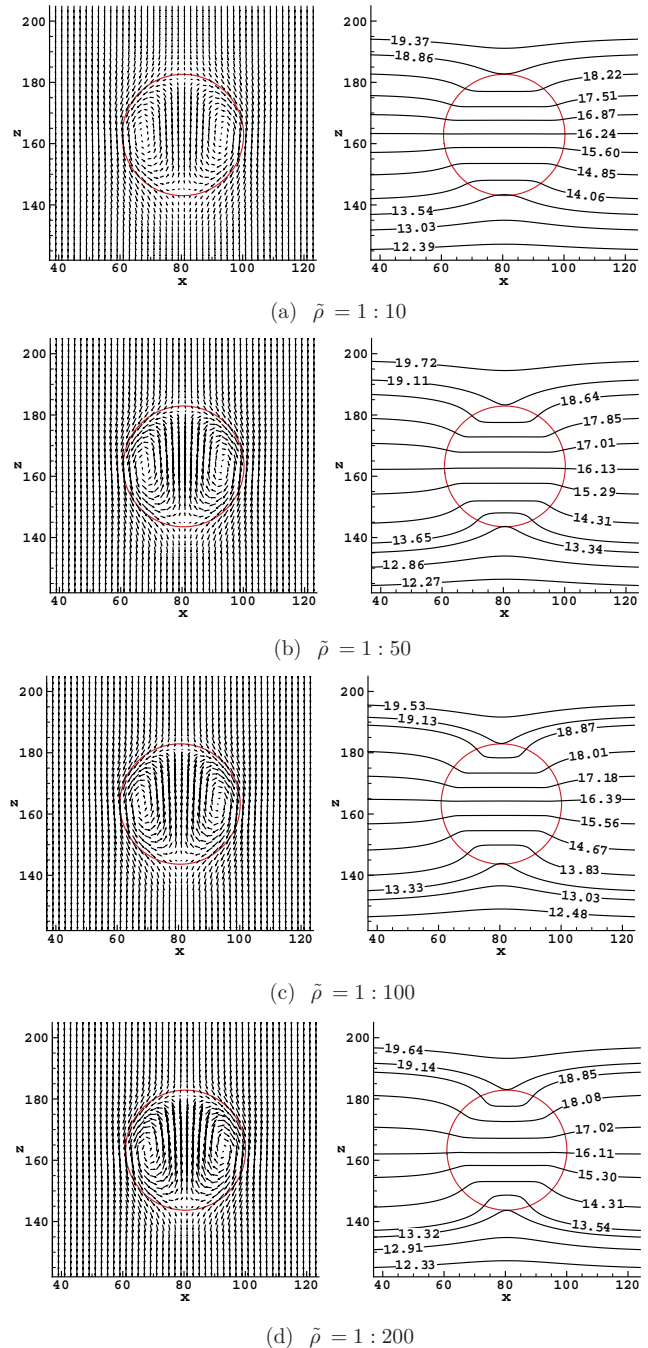
FIG. 9. (Color online) Velocity vectors (the left figures) and temperature fields (the right figures) around the migrating bubble in the x-z meridian plane at (a) $\tilde{\rho} = 10$, (b) $\tilde{\rho} = 50$, (c) $\tilde{\rho} = 100$, and (d) $\tilde{\rho} = 200$. Note that the velocity vectors are plotted in a reference frame moving with the bubble.

marching to obtain temperature field, which is related to the interfacial tension by the equation of state. The proposed model is first validated against the analytical solutions for the thermocapillary driven convection in two superimposed fluids at negligibly small Reynolds and Marangoni numbers. It is then used to simulate thermocapillary migration of three-dimensional deformable droplet and bubble at various

Marangoni numbers and density ratios, and its capability and accuracy are further verified against the theoretical predictions.

We would like to point out that the current interest in thermocapillary flows is primarily driven by applications to digital microfluidics, such as the one investigated by Takeuchi *et al.* [9], who demonstrated experimentally that thermal gradients induced by localized laser heating could be used for noncontact bubble manipulation in a microchannel with the bubble diameter ranging from 40 to 140 μm. The effect of bubble size, fluid viscosity, and optical power on the bubble migration behavior was studied in detail. In future, this experimental work will be simulated using our proposed hybrid model, and the numerical results will be compared

qualitatively and quantitatively with their experimental observations.

APPENDIX: DERIVATION OF INTERFACIAL FORCE

Here we demonstrate that Eq. (10) can lead to Eq. (9) and vice versa. Eq. (10) can be written as

$$
\begin{aligned}
\mathbf{F}_S &= \frac{3\sqrt{2}}{4}\epsilon \boldsymbol{\nabla} \cdot [\sigma |\boldsymbol{\nabla}\phi|^2 \mathbf{I} - \sigma \boldsymbol{\nabla}\phi \otimes \boldsymbol{\nabla}\phi] \\
&= \frac{3\sqrt{2}}{4}\epsilon \left[|\boldsymbol{\nabla}\phi|^2 \boldsymbol{\nabla}\sigma + \frac{1}{2}\sigma \boldsymbol{\nabla}(|\boldsymbol{\nabla}\phi|^2) - (\boldsymbol{\nabla}\sigma \cdot \boldsymbol{\nabla}\phi)\boldsymbol{\nabla}\phi - \sigma \nabla^2\phi \boldsymbol{\nabla}\phi \right].
\end{aligned}
\tag{A1}
$$

By setting $\mathbf{n} = \frac{\boldsymbol{\nabla}\phi}{|\boldsymbol{\nabla}\phi|}$, $\kappa = \boldsymbol{\nabla}\cdot\mathbf{n}$ and $q = |\boldsymbol{\nabla}\phi|$, we can have [38]

$$
\nabla^2\phi \boldsymbol{\nabla}\phi = q^2\kappa\mathbf{n} + \tfrac{1}{2}(\mathbf{n}\cdot\boldsymbol{\nabla}q^2)\mathbf{n}.
\tag{A2}
$$

Substitution of Eq. (A2) into Eq. (A1) yields

$$
\mathbf{F}_S = \frac{3\sqrt{2}}{4}\epsilon \left[q^2\boldsymbol{\nabla}\sigma + \frac{1}{2}\sigma\boldsymbol{\nabla}q^2 - q^2(\mathbf{n}\cdot\boldsymbol{\nabla}\sigma)\mathbf{n} - q^2\sigma\kappa\mathbf{n} - \frac{1}{2}\sigma(\mathbf{n}\cdot\boldsymbol{\nabla}q^2)\mathbf{n} \right].
\tag{A3}
$$

Based on the equilibrium interface profile Eq. (3), it can be easily justified the following equality

$$
|\boldsymbol{\nabla}\phi|^2 = q^2 = \frac{1}{2\epsilon^2}(\phi^2 - 1)^2.
\tag{A4}
$$

A further computation shows that

$$
\begin{aligned}
\mathbf{F}_S &= \frac{3\sqrt{2}}{4}\epsilon \left\{ q^2(\mathbf{I} - \mathbf{n}\otimes\mathbf{n})\cdot\boldsymbol{\nabla}\sigma + \frac{1}{2}\sigma\boldsymbol{\nabla}q^2 - q^2\sigma\kappa\mathbf{n} - \frac{1}{2}\sigma\mathbf{n}\cdot\boldsymbol{\nabla}\left[\frac{1}{2\epsilon^2}(\phi^2-1)^2\right]\mathbf{n} \right\} \\
&= \frac{3\sqrt{2}}{4}\epsilon \left[q^2(\mathbf{I} - \mathbf{n}\otimes\mathbf{n})\cdot\boldsymbol{\nabla}\sigma + \frac{1}{2}\sigma\boldsymbol{\nabla}q^2 - q^2\sigma\kappa\mathbf{n} - \sigma\frac{1}{\epsilon^2}(\phi^2-1)\phi(\mathbf{n}\cdot\boldsymbol{\nabla}\phi)\mathbf{n} \right] \\
&= \frac{3\sqrt{2}}{4}\epsilon \left[q^2(\mathbf{I} - \mathbf{n}\otimes\mathbf{n})\cdot\boldsymbol{\nabla}\sigma + \frac{1}{2}\sigma\boldsymbol{\nabla}q^2 - q^2\sigma\kappa\mathbf{n} - \sigma\frac{1}{\epsilon^2}(\phi^2-1)\phi q\mathbf{n} \right] \\
&= \frac{3\sqrt{2}}{4}\epsilon \left[q^2(\mathbf{I} - \mathbf{n}\otimes\mathbf{n})\cdot\boldsymbol{\nabla}\sigma + \frac{1}{2}\sigma\boldsymbol{\nabla}q^2 - q^2\sigma\kappa\mathbf{n} - \sigma\frac{1}{\epsilon^2}(\phi^2-1)\phi\boldsymbol{\nabla}\phi \right] \\
&= \frac{3\sqrt{2}}{4}\epsilon \left[q^2(\mathbf{I} - \mathbf{n}\otimes\mathbf{n})\cdot\boldsymbol{\nabla}\sigma + \frac{1}{2}\sigma\boldsymbol{\nabla}q^2 - q^2\sigma\kappa\mathbf{n} - \frac{1}{2}\sigma\boldsymbol{\nabla}\frac{1}{2\epsilon^2}(\phi^2-1)^2 \right] \\
&= \frac{3\sqrt{2}}{4}\epsilon q^2[(\mathbf{I} - \mathbf{n}\otimes\mathbf{n})\cdot\boldsymbol{\nabla}\sigma - \sigma\kappa\mathbf{n}].
\end{aligned}
\tag{A5}
$$

Therefore, we get Eq. (9). This indicates that Eqs. (9) and (10) are equivalent.

[1] L. E. Scriven and C. V. Sternling, Nature (London) **187**, 186 (1960).

[2] P. H. Hadland, R. Balasubramaniam, G. Wozniak, and R. S. Subramanian, Exp. Fluids **26**, 240 (1999).

[3] Q. Kang, H. L. Cui, L. Hu, and L. Duan, Microgravity Sci. Technol. **20**, 67 (2008).

[4] K. Kotz, K. Noble, and G. Faris, Appl. Phys. Lett. **85**, 2658 (2004).

[5] C. N. Baroud, J.-P. Delville, F. Gallaire, and R. Wunenburger, Phys. Rev. E **75**, 046302 (2007).

[6] C. Baroud, M. Robert de Saint Vincent, and J.-P. Delville, Lab Chip **7**, 1029 (2007).

[7] A. T. Ohta, A. Jamshidi, J. K. Valley, H.-Y. Hsu, and M. C. Wu, Appl. Phys. Lett. **91**, 074103 (2007).

[8] M. Robert de Saint Vincent, R. Wunenburger, and J.-P. Delville, Appl. Phys. Lett. **92**, 154105 (2008).

[9] H. Takeuchi, M. Motosuke, and S. Honami, in *Proceedings of the ASME 2009 7th International Conference on Nanochannels, Microchannels and Minichannels, June 22–24, 2009, Pohang, South Korea* (ASME, New York, 2009), pp. 1023–1030.

[10] M. Robert de Saint Vincent and J.-P. Delville, Phys. Rev. E **85**, 026310 (2012).

[11] T. Thorsen, R. W. Roberts, F. H. Arnold, and S. R. Quake, Phys. Rev. Lett. **86**, 4163 (2001).

[12] S. L. Anna and H. C. Mayer, Phys. Fluids **18**, 121512 (2006).

[13] P. Garstecki, M. J. Fuerstman, H. A. Stone, and G. M. Whitesides, Lab Chip **6**, 437 (2006).

[14] T. Fu, D. Funfschilling, Y. Ma, and H. Z. Li, Microfluid. Nanofluid. **8**, 467 (2010).

[15] M. Pollack, R. Fair, and A. Shenderov, Appl. Phys. Lett. **77**, 1725 (2000).

[16] J. Schwartz, J. Vykoukal, and P. Gascoyne, Lab Chip **4**, 11 (2004).

[17] D. Chatterjee, H. Shepherd, and R. Garrell, Lab Chip **9**, 1219 (2009).

[18] T. Jun and C. Kim, J. Appl. Phys. **83**, 5658 (1998).

[19] A. A. Darhuber, J. P. Valentino, J. M. Davis, S. M. Troian, and S. Wagner, Appl. Phys. Lett. **82**, 657 (2003).

[20] R. H. Farahi, A. Passian, T. L. Ferrell, and T. Thundat, Appl. Phys. Lett. **85**, 4237 (2004).

[21] J.-P. Delville, M. Robert de Saint Vincent, R. Schroll, H. Chraïbi, B. Issenmann, R. Wunenburger, D. Lasseux, W. Zhang, and E. Brasselet, J. Opt. A-Pure Appl. Opt. **11**, 034015 (2009).

[22] R. S. Subramanian and R. Balasubramaniam, *The Motion of Bubbles and Drops in Reduced Gravity* (Cambridge University Press, Cambridge, 2001).

[23] M. Robert de Saint Vincent and J.-P. Delville, in *Advances in Microfluidics*, edited by R. T. Kelly (InTech, Rijeka, Croatia, 2012), pp. 3–28.

[24] D. Juric and G. Tryggvason, J. Comput. Phys. **123**, 127 (1996).

[25] W. Shyy, R. W. Smith, H. S. Udaykumar, and M. M. Rao, *Computational Fluid Dynamics with Moving Boundaries* (Taylor & Francis, Washington, DC, 1996).

[26] X. He, S. Chen, and R. Zhang, J. Comput. Phys. **152**, 642 (1999).

[27] H.-Y. Chen, D. Jasnow, and J. Viñals, Phys. Rev. Lett. **85**, 1686 (2000).

[28] S. Succi, *The Lattice Boltzmann Equation for Fluid Dynamics and Beyond* (Oxford University Press, Oxford, 2001).

[29] X. He and L.-S. Luo, Phys. Rev. E **55**, R6333 (1997).

[30] A. K. Gunstensen, D. H. Rothman, S. Zaleski, and G. Zanetti, Phys. Rev. A **43**, 4320 (1991).

[31] X. Shan and H. Chen, Phys. Rev. E **47**, 1815 (1993).

[32] M. R. Swift, E. Orlandini, W. R. Osborn, and J. M. Yeomans, Phys. Rev. E **54**, 5041 (1996).

[33] T. Lee and C.-L. Lin, J. Comput. Phys. **206**, 16 (2005).

[34] T. Lee and L. Liu, J. Comput. Phys. **229**, 8045 (2010).

[35] H. Liu, Y. Zhang, and A. J. Valocchi, J. Comput. Phys. **231**, 4433 (2012).

[36] M. Latva-Kokko and D. H. Rothman, Phys. Rev. E **71**, 056702 (2005).

[37] J. Kim, Commun. Comput. Phys. **12**, 613 (2012).

[38] C. Liu and J. Shen, Physica D **179**, 211 (2003).

[39] J. W. Cahn and J. E. Hilliard, J. Chem. Phys. **28**, 258 (1958).

[40] T. Zhang and Q. Wang, Commun. Comput. Phys. **7**, 362 (2010).

[41] V. E. Badalassi, H. D. Ceniceros, and S. Banerjee, J. Comput. Phys. **190**, 371 (2003).

[42] C. Ma and D. Bothe, Int. J. Multiphase Flow **37**, 1045 (2011).

[43] H. Ding, P. D. Spelt, and C. Shu, J. Comput. Phys. **226**, 2078 (2007).

[44] Q. Li, K. H. Luo, Y. J. Gao, and Y. L. He, Phys. Rev. E **85**, 026704 (2012).

[45] T. Lee, Comput. Math. Appl. **58**, 987 (2009).

[46] P. Lallemand and L.-S. Luo, Phys. Rev. E **68**, 036706 (2003).

[47] H. Huang, T. Lee, and C. Shu, Int. J. Numer. Meth. Fluids **53**, 1707 (2007).

[48] F. Verhaeghe, B. Blanpain, and P. Wollants, Phys. Rev. E **75**, 046705 (2007).

[49] A. Tiribocchi, N. Stella, G. Gonnella, and A. Lamura, Phys. Rev. E **80**, 026701 (2009).

[50] B. Pendse and A. Esmaeeli, Int. J. Therm. Sci. **49**, 1147 (2010).

[51] N. Young, J. Goldstein, and M. Block, J. Fluid Mech. **6**, 350 (1959).

[52] D. Oliver and K. Witt, J. Colloid Interface Sci. **164**, 263 (1994).

[53] S. Welch, J. Colloid Interface Sci. **208**, 500 (1998).

[54] N. Shankar and R. S. Subramanian, J. Colloid Interface Sci. **123**, 512 (1988).

[55] Y. Wang, X. Lu, L. Zhuang, Z. Tang, and W. Hu, Acta Astronaut. **54**, 325 (2004).

[56] Z. Yin, P. Gao, W. Hu, and L. Chang, Phys. Fluids **20**, 082101 (2008).

[57] M. Hill, Proc. R. Soc. Lond. **55**, 219 (1894).

[58] L. Amaya-Bower and T. Lee, Comput. Fluids **39**, 1191 (2010).

[59] D. Chiappini, G. Bella, S. Succi, F. Toschi, and S. Ubertini, Commun. Comput. Phys. **7**, 423 (2010).

[60] M. Gross, N. Moradi, G. Zikos, and F. Varnik, Phys. Rev. E **83**, 017701 (2011).

[61] Z. Guo, C. Zheng, and B. Shi, Phys. Rev. E **83**, 036707 (2011).

[62] Q. Lou, Z. L. Guo, and B. C. Shi, Europhys. Lett. **99**, 64005 (2012).